Ceramic ZnO-SnO$_2$-Fe$_2$O$_3$ Powders and Coatings -Effective Photogenerators of Reactive Oxygen Species

Larisa Khomutinnikova [1,*], Sergey Evstropiev [1,2,3,*], Igor Meshkovskii [1], Igor Bagrov [2] and Valery Kiselev [2]

[1] Technical Physics Department, ITMO University, Saint-Petersburg 197101, Russia; igorkm@niuitmo.ru
[2] Vavilov State Optical Institute, Saint-Petersburg 192171, Russia
[3] Saint-Petersburg State Technological Institute, Technical University, Saint-Petersburg 190013, Russia
* Correspondence: lesnykhlara@gmail.com (L.K.); evstropiev@bk.ru (S.E.)

Abstract: Ceramic ZnO-SnO$_2$-Fe$_2$O$_3$ powders and transparent coatings on glasses prepared using the non-isothermal polymer-salt method demonstrate a strong ability to generate chemically active oxygen species under UV and visible irradiation. Crystal structures and morphologies of these materials were studied using the XRD and the SEM analysis. It was found that there are significant differences in the crystal structure of ceramic powders and thin coatings. The powders consist of randomly oriented oxide nanocrystals of size ~47 nm. The strong orientation of the ZnO nanocrystals due to their interaction with the glass substrate is observed in the coating structure. Experimental data show that thin ceramic coatings are transparent (~90%) in the visible spectral range and the band gap of the ceramic material is 3.44 eV. The band gap value of this multi-component ceramic material is described sufficiently using Verlag's law. Ceramic powders and coatings demonstrate the intensive photogeneration of reactive oxygen species, both in liquid and air. High photocatalytic activity of ZnO-SnO$_2$-Fe$_2$O$_3$ ceramic coatings and powders was observed upon the oxidation of the diazo dye, Chicago Sky Blue. In the presence of transparent photocatalytic coating, the value of the constant rate of the dye photodecomposition was high (k = 0.056 min^{-1}). It was found that, in spite of their short life time, photogenerated reactive oxygen species demonstrate the ability to decompose dye molecules located up to a distance of 0.5 mm from the surface of ceramic coating. Obtained experimental results suggest that the prepared ceramic materials are promising for different practical applications of the photocatalytic materials.

Keywords: ceramics; coating; photocatalysis; crystal

1. Introduction

Photocatalytic materials are used in many different practical applications (water and air purification, sensors, water splitting, etc.) and are the object of intensive investigations [1–14]. Many oxide semiconductor materials are effective photocatalysts, demonstrate antibacterial activity and have an excellent thermal stability and chemical durability.

Ceramic materials (powders and coatings) based on ZnO are very effective photocatalysts [2–14] which have been successfully tested in industrial conditions [1]. Modification of the ZnO ceramic materials using other oxides additions provides a significant enhancement to its photocatalytic and bactericidal characteristics [3–8]. These additions decrease the size of ZnO crystals, modify the crystal structure and morphology of the ZnO ceramic materials and increase their specific surface areas.

The reaction between reactive oxygen species (ROS) and organic compounds is the key process in photocatalysis [10,15–17]. Therefore, the high ability of the photogeneration of chemically active oxygen species is very important for photocatalytic materials. The effectiveness of ROS photogeneration depends on the chemical composition of the photocatalyst, its structure and morphology as well as on the parameters of excited radiation (intensity, wavelength, etc.) [18–20]. It is known that the chemical reactive activity of ROS is very

high and, therefore their lifetime in the liquid or gas phases is short [16,21,22]. Therefore, it is believed that often photogenerated ROS decompose only organic molecules adsorbed on the surface of the photocatalysts, [23] and hence the photocatalysis rate cannot exceed the adsorption rate. However, the experimental data described in [16,24,25] show that organic decomposition can be observed in gas or liquid phases at some distance from the photocatalyst surface. The additional study of this phenomenon is important for scientific knowledge on practical photocatalytic applications.

Chemical composition, structure and morphology of photocatalysts determine the spectral diapason of the light which can excite a semiconductor material, its specific surface area, adsorption properties and photocatalytic activity. It was found [2,6–9] that materials consisting of semiconductor nanoparticles with specific shapes, such as nanorods, nanowires and "flowers", exhibit high photocatalytic properties.

Photocatalytic activity of semiconductors depends on the intensity of the exciting light. This phenomenon is determined by the competition between different processes occurring in the material after its light excitation and the generation of electron-hole pairs [18,19]. The photogenerated charges recombination play a negative role in photocatalysis. The alternative process is the ROS formation on the material surface. The ratio of these competitive processes remains constant at the small light intensity and the dependence of the photocatalysis rate v from light intensity I is linear ($v = kI$) [18]. The increase in light intensity leads to a more significant growth of the recombination process and the dependence $v = f(I)$ transfers to the view $v = kI^n$ $n < 1$.

Multicomponent photocatalysts consisting of two or more closely packed different semiconductor particles are used in photocatalysis. The application of these semiconductor heterostructures allows to decrease the possibility of the recombination of photogenerated electron-hole pairs by the spatial separation of charges. It was found that the application of different heterostructures (ZnO-SnO_2 [3,4]; ZnO-Fe_2O_3 [6]; ZnO-TiO_2 [5]) provides the increase in the effectiveness of photocatalysis [3–6].

It is known [26,27] that the crystalline structure and the morphology of ceramic coatings and powders differ significantly due to the interaction of coating material and the substrate surface. This interaction inhibits the crystallization process [26] and stimulates the texture formation [14,27,28] in the coating materials. Therefore, besides the difference in the thickness of photocatalytic layers between thin ceramic coating and powder, the features of crystal structures and morphologies of these ceramics can have an influence on their photocatalytic properties. In spite of small thickness, ceramic coatings demonstrate photocatalytic properties [4,5,14,20,29–32], although in some cases the photocatalysis rate is low [31].

ZnO-SnO_2 ceramic materials are one of the most effective ZnO-based photocatalysts [3,4,7,28]. ZnO and SnO_2 have relatively high band gap values (3.37 and 3.6 eV, respectively [33]), and demonstrate high photocatalytic properties under UV irradiation [4,29]. Different approaches, such as the application of some additions (Ag [9,10,34], Co [29], etc.) or the structural engineering [7], have been developed to increase the photocatalytic properties of these materials in the visible spectral range.

Many methods have been developed for the preparation of nanocrystalline ceramic ZnO-SnO_2 photocatalysts: polymer-salt method [4], sol-gel technique [33,35], hydrothermal method [36], spray pyrolysis [37], etc. Polymer-salt synthesis is a facile and an effective method widely used in the preparation of different ZnO-based nanomaterials and thin ceramic coatings [4,7,16,25–28]. Photocatalytic ZnO-SnO_2-Fe_2O_3 powders consisting of "flower"-like particles have been synthesized using the non-isothermal polymer-salt synthesis in [7]. It was exposed that the small additions of Fe_2O_3 provides a significant increase in photocatalytic properties of ZnO-SnO_2 powder materials.

Thin photocatalytic ceramic films are required for some important practical application, such as transparent "self-cleaning" and bactericidal coatings on displays surfaces, medical and laboratory equipment, etc. Clearly, for such applications ceramic coatings should demonstrate high transparency (≥90%) in the visible spectral range. ZnO-SnO_2 thin

coatings exposed high transparency in the visible spectral range [4]. Fe_2O_3 has a relatively small band gap value (2.0 eV [38]) and the addition of this component to ZnO-SnO_2 compositions can significantly affect the transparency of ceramic coatings. Therefore, the possibility of forming photocatalytic ZnO-SnO_2-Fe_2O_3 coatings with high transparency was not obvious in the beginning.

The aim of this work is the analyses of polymer-salt synthesis of thin ceramic ZnO-SnO_2-Fe_2O_3 coating and powders, detailed characterization of these materials and the comparison of their crystal structure, morphology and photocatalytic properties.

2. Materials and Methods

The polymer-salt technique, described in detail in [4,7,23,26,29], was used for the preparation of ceramic powder and coatings. Aqueous solutions of $Zn(NO_3)_2$, $SnCl_2$ and $FeCl_3$ in pre-determined volumes were mixed at room temperature with the solution of high-molecular polyvinylpyrrolidone (PVP, M_w = 1,300,000; Sigma-Aldrich) in ethanol. The additions of PVP are used for the stabilization of the forming nanoparticles [7,16]. The list of raw materials used is given in Table 1.

Table 1. List of used raw materials.

Compound	Supplier	Specification
$Zn(NO_3)_2 \cdot 6\, H_2O$	Neva Reactive Co., (Neva Reactive, Saint-Petersburg, Russia)	UPCR-5106.F00250 CAS: 0196-18-6
$SnCl_2 \cdot 2\, H_2O$	MERCK	MERCK-1078150250 CA S: 10025-69-1 ACS. ISO. Reag. PhEur.
$FeCl_3 \cdot 6\, H_2O$	Neva Reactive Co., (Neva Reactive, Saint-Petersburg, Russia)	ACROS-217091000 CAS: 10025-77-1
Polyvinylpyrrolidone	Sigma-Aldrich	K30; CAS: 9003-39-8
Chicago Sky Blue 6 B	Sigma-Aldrich	CAS: 2610-05-1

The mixed solution was dried at 70 °C for 24 h to prepare the powders. Then, obtained polymer-salts composite were subjected to a thermal treatment at 550 °C for 2 h.

The deposition of thin coatings on the glass samples was carried out using the dipping method at room temperature. This technique leads to the formation of thin uniform composite coatings composed of PVP polymer matrix with small salt particles. After deposition, coated samples were dried at room temperature for 24 h and were calcined at 550 °C for 2 h. Nominal chemical compositions of the ceramic powder and thin coating were the same: ZnO 95 mol.%; SnO_2 3 mol.%; and Fe_2O_3 2 mol.%.

The crystal structure of prepared gels and ceramic samples were studied using the XRD method which incorporates the Rigaku Ultima IV device. The diffraction patterns were scanned from 20° to 50° (2θ). Based on the obtained XRD data, we estimated the crystal sizes using the Scherrer formula:

$$d = \frac{K \times \lambda}{\beta \times cos\theta} \tag{1}$$

where d is the average crystal size; K is the dimensionless particle shape factor (for spherical particles K = 0.9); λ is the X-ray wavelength (λ (CuKα = 1.5418 Å); β—is the width of the reflection at half height (in radians, and in units of 2θ); and θ is the diffraction angle.

The morphology and chemical composition of the prepared samples were studied using the SEM and the energy-dispersive analysis which is equipped with the electronic microscope TESCAN VEGA3, an Advanced Aztec Energy system (Oxford Instruments,

Oxford, UK). EDS analysis showed that the difference between nominal and analytical chemical compositions of prepared ceramic materials did not exceed 10%.

Double beam UV–Vis spectrophotometer, Perkin-Elmer Lambda 650, was used for measuring the absorption spectra. The quartz cuvette (thickness 10 mm) was used for solutions measurements.

Photoluminescence spectra, near the IR spectral region were measured upon excitation by the radiation of LEDs (HPR40E set) with emission bands maximums at 370 nm and 405 nm, using the SDH-IV spectrometer (SOLAR Laser Systems).

For photocatalytic tests of the thin coatings, we used the experimental technique which is similar to that used earlier in [4,16]. Diazo dye, Chicago Sky Blue (CSB, Sigma Aldrich), was used in the photocatalytic experiments as a model organic contaminant. Spectral properties of CSB were described in detail in [39]. This dye was often used earlier for the characterization of the photocatalytic properties of different materials [4,9,40–42].

Small glass sheets with coatings having a surface area about 2 cm^2 and a thickness of 0.5 mm were put into a quartz cuvette. Then the cuvette was filled using a CSB solution and was subjected to UV irradiation by using a high-pressure mercury lamp (DRT-250, STK-Light, Moscow, Russia). The radiation energy density was 0.25 W/cm^2 during the photocatalytic test for CSB photodecomposition in the solutions.

Photocatalytic experiments were carried out to study the effect of photogenerated ROS on CSB molecules located at some distance from the photoactive ceramic coating. The scheme of this experiment is shown in Figure 1. Thin CSB coating from the alcohol solution was deposited on the glass plate and was then dried in air atmosphere. The glass specimens with dye and ceramic coatings were disposed one above the other at the distance 0.5 mm. The irradiation was carried out for 5 min from the side of the glass sample with the ceramic coating. Each photocatalytic test was repeated 3 ÷ 4 times and the difference obtained between the experimental results of similar tests did not exceed 10%.
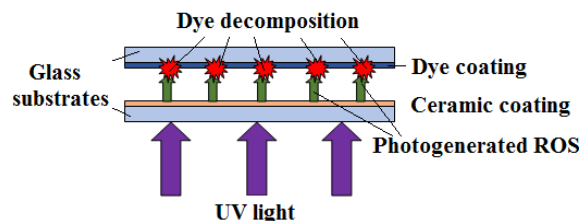

**Figure 1.** Scheme of photocatalytic experiments in air atmosphere.

3. Results

3.1. XRD Analysis

XRD analysis showed the significant differences in the structure of the prepared ceramic coatings and powders. Intensive peaks of hexagonal ZnO crystals are observed in the XRD pattern of ceramic powder (Figure 2a). A few small peaks of the same ZnO crystals are observed in the XRD patterns of ceramic coating. The average size of the ZnO crystals in the powder, calculated using Scherer's formula, is 47 nm. In addition to the peaks of ZnO crystals, small peaks of SnO_2 and Zn_2SnO_4 crystals are observed in XRD pattern of ceramic powder (Figure 2a).

Relative intensities of ZnO peaks in the diffraction pattern of ceramic powder are fully corresponding to the standard values (JCPDS card No. 36-1451). Based on the experimental results, the relative ZnO peaks intensities in the XRD patterns of ceramic powders and coatings, were calculated (Table 2). The data obtained indicate the significant differences in the crystal structures of ceramic powder and thin coating. In the powder, there is no preferred crystal orientation and relative peaks intensities are close to standard values (Table 2). In contrast, the small coating thickness and the strong interaction of forming crystals with the substrate surface determined the preferable orientation of ZnO crystals

along (002) direction (Figure 2b). This phenomenon was described earlier in ZnO-based coatings prepared using different methods [11,14,28,37,43].
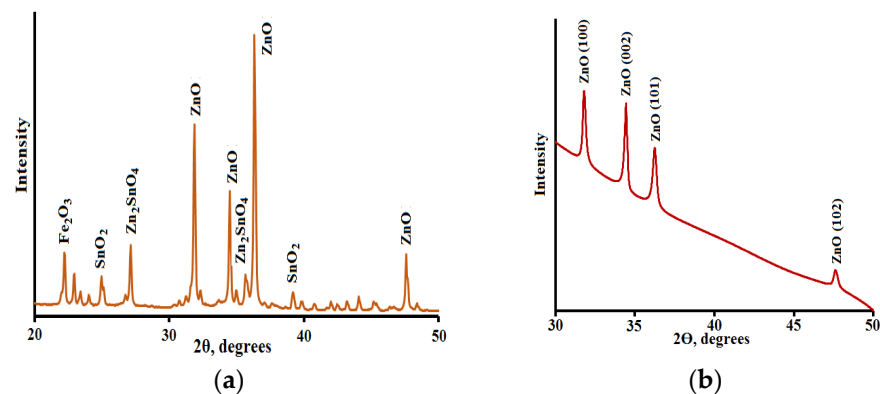
Figure 2. Diffraction patterns of ceramic powder (**a**) and thin ceramic coating on the glass (**b**).

In diffraction patterns of ceramic coating, ZnO crystals peaks positions are very close to standard values (JCPDS card No. 36-1451) (Table 2). The peaks position of these crystals in the XRD pattern of ceramic powder somewhat differ from standard values, however, this difference is not significant. Such variations of peaks positions are observed in the XRD patterns of ZnO crystals prepared using low-temperature methods [13].

Table 2. Relative peaks intensities and peaks positions of ZnO crystals in ceramic powders and coatings.

Planes (hkl) Planes	Relative Peaks Intensities			Peaks Positions 2Q, Degrees		
	JCPDS Card No. 36-1451	Ceramic Powder	Ceramic Coating	JCPDS Card No. 36-1451	Ceramic Powder	Ceramic Coating
(100)	57	55	82	31.770	31.85	31.78
(002)	44	36	100	34.422	34.50	34.42
(101)	100	100	70	36.253	36.30	36.21

Thus, the XRD data indicate the formation of ZnO crystals as the main crystal phase in the obtained powder and coating.

3.2. SEM Analysis

Figure 3 demonstrates a SEM photo of the ceramic powder (a) and thin coating (b). The powder consists of randomly oriented microscopic particles which have the the shape of hexagonal rods. The structure of ceramic coating contains small particles with a size of about 150 nm (Figure 3b).

Figure 4 shows the transmittance spectra of the initial glass sample without coatings and samples with ceramic ZnO-SnO_2-Fe_2O_3 coatings deposited on one or two sides of the glass plates. The deposition of the coatings decrease the transparency in glass samples. Significant transparency reduction is observed in the UV spectral range that is related to the fundamental absorption of the semiconductor coating material. The observed light absorption in the spectral range $400 \div 420$ nm, indicates the possibility of the excitation of ceramic coatings by blue light.

At the same time, it is worth noticing that the transparency decrease observed after the coating deposition on one side of the glass plate do not exceed a few percents in the visible spectral range ($420 \div 670$ nm). This fact indicates the possibility for the practical application of this transparent coating on the surface of different displays, windows, medical instruments, and other objects.
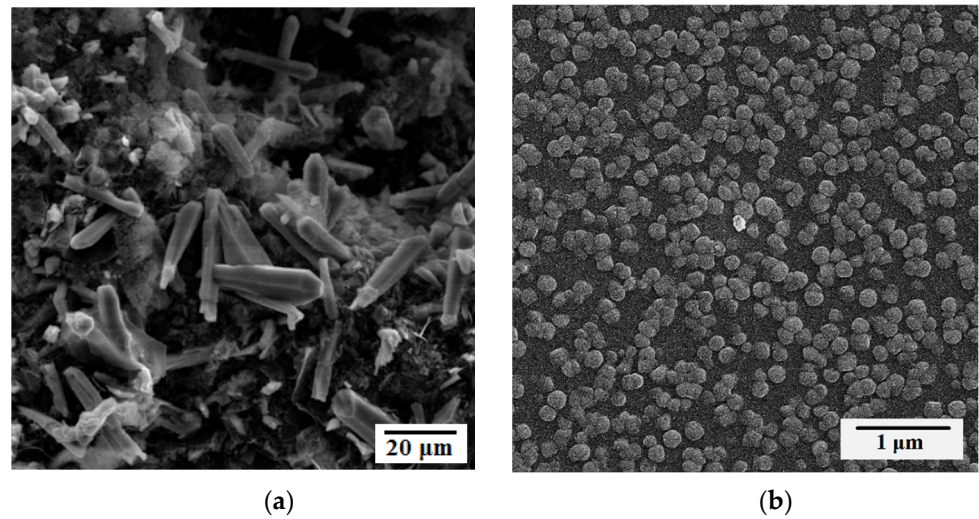
(a) (b)

Figure 3. SEM images of the ceramic powder (**a**) and thin coating (**b**).
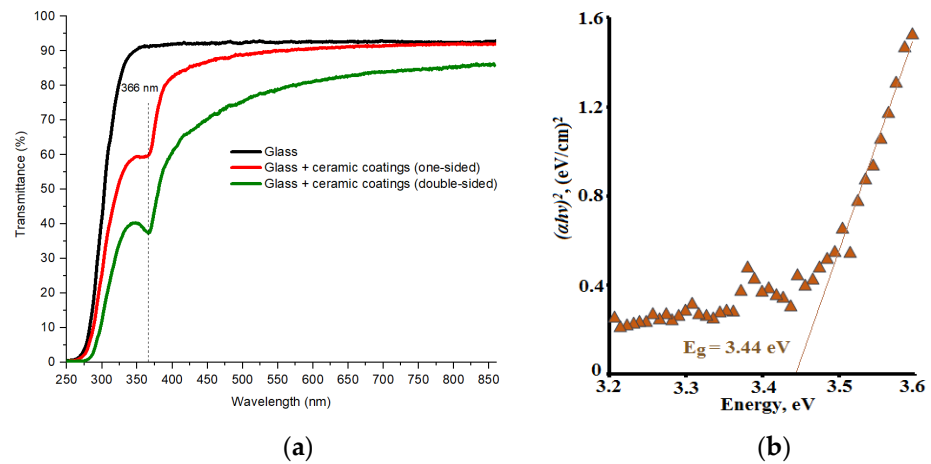

(a) (b)

Figure 4. (**a**) Transmittance spectra of glass sample and glass samples with ceramic coatings; (**b**) The dependence $(\alpha h\nu)^2 = f(h\nu)$ for the coating material.

The intensive absorption band with $\lambda_{max} = 366$ nm, observed in the spectra of coated samples, is the characteristic excitonic absorption band of ZnO nanoparticles [44]. The appearance of this band in the spectra of coated sample is explained by the high content of ZnO crystals in the structure of ceramic coating.

The band gap values of the synthesized coatings were estimated using the Tauc's equation [45], which can be written for direct semiconductors as:

$$(\alpha h\nu)^2 = A(h\nu - E_g) \tag{2}$$

where $h\nu$—photon energy, E_g—band gap value, A—constant, α—absorption coefficient. The plotting of the graphs $(\alpha h\nu)^2$ vs. $h\nu$ was used for the determination of E_g value of the coating material (Figure 3b).

Obtained E_g value is 3.44 eV, which is higher than the E_g of macroscopic ZnO crystals ($E_g^{ZnO} \sim 3.37$ eV [33,44,46]). The bang gap values of multicomponent semiconductors are estimated often using Verlag's law, which describes the dependence of the semiconductor band gap value on b parameter (parameter of a non-linearity) and molar ratio between its components.

The bang gap values of the multicomponent ZnO-based semiconductors were described sufficiently using Verlag's law at $b = 0$ [26,47,48]. For **(100-x-y)** ZnO-**x**SnO$_2$-**y**Fe$_2$O$_3$

material with x molar fraction of SnO_2, y molar fraction of Fe_2O_3 and $b = 0$, Verlag's law can be expressed with the equation:

$$E_g^{(ZnO\text{-}SnO_2\text{-}Fe_2O_3)} = xE_g^{SnO_2} + yE_g^{Fe_2O_3} + (1\text{-}x\text{-}y)E_g^{ZnO} \tag{3}$$

where $E_g^{(ZnO\text{-}SnO_2\text{-}Fe_2O_3)}$ is a coating material band gap value, $E_g^{SnO_2}$, E_g^{ZnO} and $E_g^{Fe_2O_3}$ are band gap values of SnO_2, ZnO and Fe_2O_3, respectively. The substitution of molar ratios of oxides and their band gap values ($E_g^{ZnO} \sim 3.37$ eV [33,44,46], $E_g^{SnO_2} \sim 3.6$ eV [33], $E_g^{Fe_2O_3} = 2.0$ eV [38]) into Equation (2) gives $E_g^{(ZnO\text{-}SnO_2\text{-}Fe_2O_3)} = 3.33$ eV that is less than the value obtained from the spectral measurements (3.44 eV). This fact can be related to some deviation of the parameter b from 0 and to the small size of the semiconductor crystals in the coating and the effect of quantum confinement on them.

Photoluminescence spectra of the ceramic coating in NIR spectral range are exposed in Figure 5. The intensive luminescence band characteristic of singlet oxygen ($^1\Delta_g\text{--}\,^3\Sigma_g$ electronic transition [49]) is observed in the spectra at different light excitations.
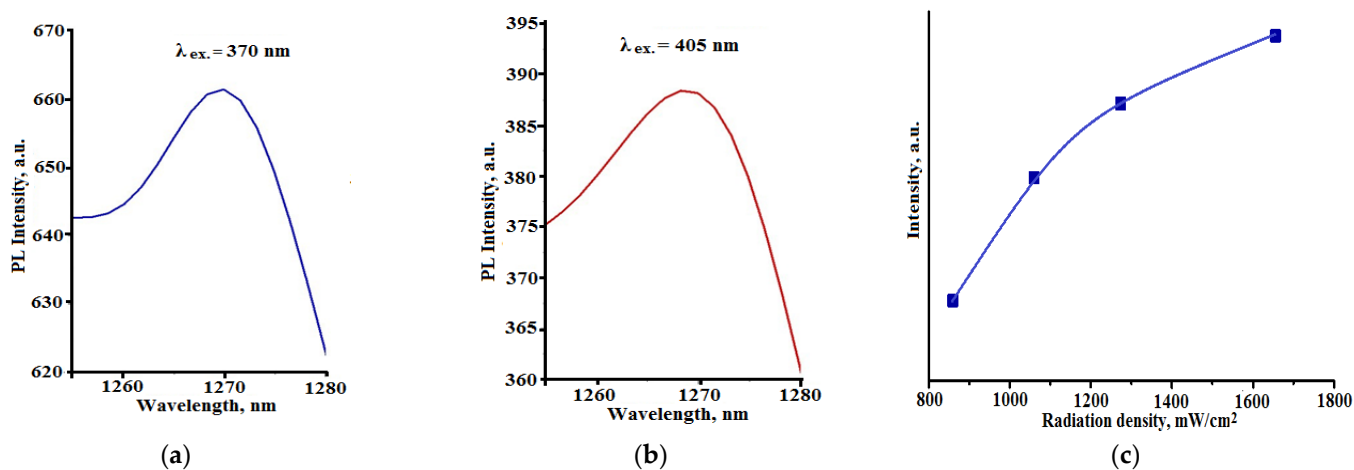
Figure 5. Photoluminescence spectra of ceramic coating (**a,b**). Dependence of the luminescence intensity from the excited radiation density (**c**).

It is important to notice that the singlet oxygen photogeneration by the ceramic coating occurs under visible light irradiation (λ_{ex} = 405 nm) (Figure 5b). The increase in visible light intensity enhances significantly during this process (Figure 5c). The obtained dependence of the luminescence band (λ = 1270 nm) intensity I_{SO}, from the intensity of excited visible irradiation (λ_{ex} = 405 nm) I_{ex} is not linear and can be described with the expression:

$$I_{SO} = I_{ex}^\beta, \text{ where } (0 \leq \beta < 1) \tag{4}$$

It is worth noting that the observed behavior of this dependence is similar to the dependencies of the photocatalytic activities of different semiconductors from the intensities of excited light irradiation reported in [19,20,50]. The non-linear behavior of the dependence is determined by the significant increase in the recombination of photogenerated electron-hole pairs due to the growth of the excited radiation intensity [19].

Active ROS photogeneration using prepared ceramic materials determines their high ability to decompose organic compounds in solutions and in the gaseous phase. Figure 6a shows the kinetic dependencies of CSB dye adsorption from the solution on the surface of the powder (curve 2) and its photodecomposition in the solution under UV irradiation (curves 1, 3, 4).

Figure 6a also shows kinetics dependencies of the dye photodecomposition in solutions. The rate of this process without ceramic photocatalysts additions is low (curve 1, Figure 6a), and less than 20% of the dye molecules are decomposed in 30 min. After UV

irradiation, the dye solution without photocatalytic additions remains in the bright blue color (photo 1, inset in Figure 6a).

The comparison of curves 1 and 2 show that the addition of the glass plate with thin ceramic coating remarkably accelerates CSB decomposition in the solution and more than 50% of the CSB molecules are oxidized in 5 min. The remarkable discoloration of the CSB solution was observed after 30 min of UV irradiation (photo 2, inset in Figure 6b). These experimental data show that this coating demonstrates higher photocatalytic activity than $ZnO-Er_2O_3$, $ZnO-Sm_2O_3$ and $ZnO-SnO_2$ coatings prepared earlier, using the same polymer-salt method described in [4,26].

The additions of ceramic powders or the glass sample with photocatalytic ceramic coating significantly accelerate CSB photodecomposition. The ceramic powder rapidly adsorbed dye molecules from the solution and after 5 min more than 95% of them were removed from the liquid phase (curve 2, Figure 6a). The constant rate value of CSB photodecomposition in the solution using $ZnO-SnO_2-Fe_2O_3$ powder was high ($k = 0.224$ min^{-1}). Additionally, UV irradiation of the ceramic powder accelerates discoloration of the dye solution (curve 3, Figure 6a). The addition of ceramic powders provides almost full discoloration of the CSB solutions after 30 min (photos 3 and 4, inset in Figure 6b).
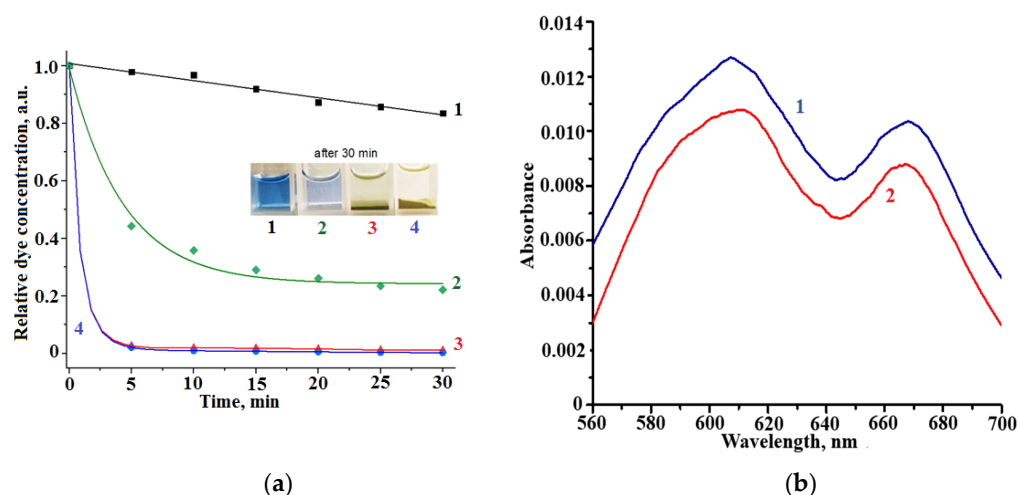
Figure 6. (**a**) Kinetics of adsorption (curve 2) and photodecomposition of CSB dye in the solution under UV irradiation (curves 1,3,4). Curve 1—Photodegradation of dye in the solution without photocatalytic addition; Curve 2—Photodegradation of dye in the solution containing the glass sample with transparent ceramic coating; Curve 4—Dye adsorption from the solution on the surface of the powder sample in the darkness; Curve 4—Photodegradation of dye in the solution with ceramic powder. Inset: Photo of dye solutions after UV treatment (samples 1,2,3) or after adsorption during 30 min. (**b**) Influence of photogenerated ROS on the absorption spectra of thin diazo dye coatings. Initial coating (curve 1); coating subjected to the action of photogenerated ROS from gas phase (curve 2).

Table 3 shows the comparison of the constant rates of CSB photodecomposition by thin ceramic coatings under UV irradiation (power density $20 \div 25$ mW/sm^2) in aqueous solutions with different photocatalytic additions. Prepared $ZnO-SnO_2-Fe_2O_3$ coating demonstrates a constant rate of CSB photodecomposition which is significantly higher than previously synthesized ZnO-based ceramic coatings.

According to the XRD data (Figure 2 and Table 3), the distortion of ZnO crystals in the coating is low and cannot significantly affect its photocatalytic activity. Therefore, this fact suggests that observed high photocatalytic activity of prepared coating can be related with its morphology (formation the texture) and/or chemical composition. The remarkable effect of ZnO crystal orientation in thin coating on its photocatalytic properties was described earlier in [14].

In contrary to the coating, some distortion of the ZnO crystals is observed in the powder (Table 2). Moreover, crystal structures of $ZnO\text{-}SnO_2\text{-}Fe_2O_3$ powders can contain some structural defects, such as oxygen vacancies and Zn interstitials [7]. These structural defects can affect the photocatalytic properties of the prepared powder.

Table 3. The comparison of the constant rates of CSB photodecomposition by thin ceramic coatings under UV irradiation (power density $20 \div 25$ mW/sm^2) in aqueous solutions with different photocatalytic additions.

Photocatalysts	Constant Rate, min^{-1}	References
ZnO 100%	0.022	[4]
ZnO 93.2 mol.% + SnO$_2$ 6.8 mol.%	0.026	[4]
ZnO 95.7 mol.% + Er$_2$O$_3$ 4.3 mol.%	0.012	[26]
ZnO 95.3 mol.% + Er$_2$O$_3$ 4.7 mol.%	0.017	[26]
ZnO 96.2 mol.% + Sm$_2$O$_3$ 3.8 mol.%	0.014	[26]
ZnO 95 mol.% + SnO$_2$ 3 mol.% + Fe$_2$O$_3$ 2 mol.%	**0.056**	**present work**

Figure 6b illustrates the photocatalytic decomposition of the thin dye coating deposited on the glass substrate by the photogenerated ROS from the gas phase. The absorption spectra of CSB thin coating deposited on glass substrate before (curve 1) and after (curve 2) the photocatalytic process are also shown in this figure. Two absorption peaks characteristic of the CSB molecules ($\lambda_{max} = 618$ nm) and their dimers ($\lambda_{max} = 670$ nm) ([39]) are observed in these spectra. ROS generated during UV irradiation of the ceramic coating decomposed some part of the CSB molecules and light absorption of the CSB coating decreased. It is worth noting that, in spite of their short life time, photogenerated ROS demonstrate the ability to decompose dye molecules located up to a distance of 0.5 mm from the surface of the photocatalytic coating.

The dye adsorption significantly changes the color of the powder from bright yellow to brown (Figure 7a,b). Additionally, UV irradiation accelerates the dye removal (curve 3, Figure 5). The color of the ceramic powder also changes after photocatalytic process within 30 min. However, this color change is somewhat smaller compared to dye adsorption without UV irradiation (Figure 7c). It is worth noticing that dye molecules are decomposed during the photocatalytic process whilst they are only concentrated on the surface of ceramic powder during the adsorption without UV irradiation.

(**a**)   (**b**)   (**c**)
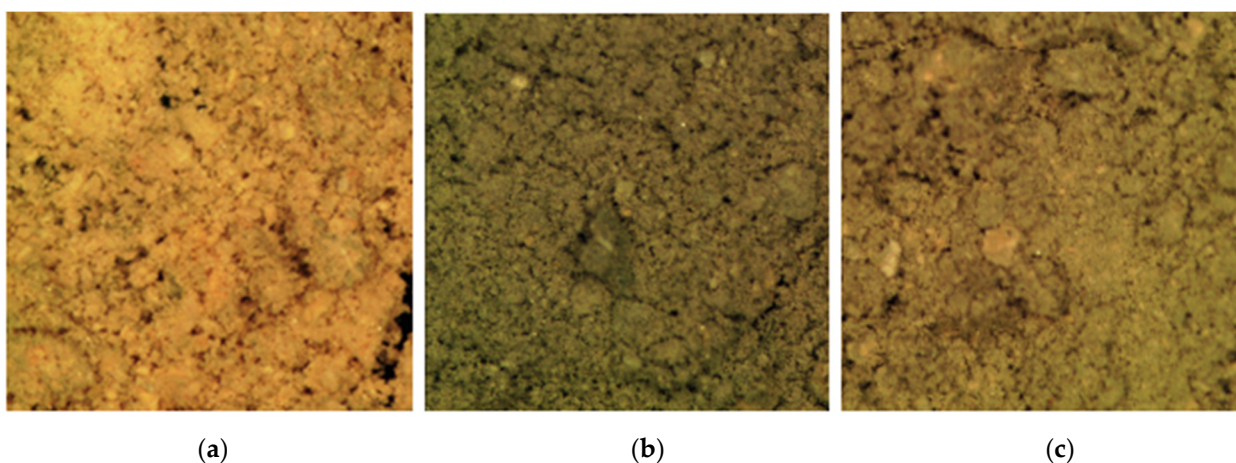
Figure 7. Photos of the surface of ceramic powders. (**a**) Initial powder; (**b**) Dried powder after dye adsorption during 30 min; (**c**) Dried powder after photocatalytic process during 30 min.

Thus, both ceramic ZnO-SnO$_2$-Fe$_2$O$_3$ powders and coatings demonstrate high adsorption activity and photocatalytic properties.

4. Conclusions

ZnO-SnO$_2$-Fe$_2$O$_3$ ceramic powders and transparent coatings with high photocatalytic properties were synthesized using the non-isothermal polymer-salt method. The crystal structures and morphologies of obtained ceramic materials were studied using the XRD and the SEM analysis.

Experimental data show that thin ceramic coatings are transparent (~90%) in the visible spectral range and the band gap of ceramic material is 3.44 eV. The band gap value of this multi-component ceramic material is described sufficiently using Verlag's law.

It was found that ceramic powders as well as thin coatings demonstrate a strong ability to generate reactive oxygen species (ROS) under UV ($\lambda_{ex.}$ = 365 nm) and visible ($\lambda_{ex.}$ = 405 nm) irradiation. The concentration of photogenerated singlet oxygen from the intensity of excited light is non-linear which is determined by the significant increase in the recombination of photogenerated electron-hole pairs due to the growth of the excited radiation intensity. ZnO-SnO$_2$-Fe$_2$O$_3$ ceramic coatings and powders demonstrate a high photocatalytic effect upon the photodecomposition of the diazo dye Chicago Sky Blue, both in the solution and in the air. It was found that, in spite of their short life time, photogenerated ROS demonstrate the ability to decompose dye molecules located up to a distance of 0.5 mm from the surface of the photocatalytic ceramic coating. Experimental data suggest that ZnO-SnO$_2$-Fe$_2$O$_3$ ceramic materials are promising for different environmental and medical applications.

References

1. Vela, N.; Calín, M.; Yáñez-Gascón, M.J.; Garrido, I.; Pérez-Lucas, G.; Fenoll, J.; Navarro, S. Photocatalytic oxidation of six endocrine disruptor chemicals in wastewater using ZnO at pilot plant scale under natural sunlight. *Environ. Sci. Pollut. Res.* **2018**, *25*, 34995–35007. [CrossRef] [PubMed]
2. Matos, R.S.; Attah-Baah, J.M.; Monteiro, M.D.S.; Costa, B.F.O.; Mâcedo, M.A.; Junior, R.S.S.; da Fonseca Filho, H.D.; Oliveira, R.M.P.B.; Ferreira, N.S. Effect of the amapá-latex chelating agent contens on the microstructure and photocatalytic properties of ZnO nanoparticles. *J. Mater. Res. Technol.* **2023**, *22*, 2673–2689. [CrossRef]
3. Palai, A.; Panda, N.R.; Sahu, D. Novel ZnO blended SnO$_2$ nanocatalysts exhibiting superior degradation of hazardous pollutants and enhanced visible photoemission properties. *J. Mol. Struct.* **2021**, *1244*, 131245. [CrossRef]
4. Evstropiev, S.K.; Lesnykh, L.V.; Karavaeva, A.V.; Nikonorov, N.V.; Oreshkina, K.V.; Mironov, L.Y.; Maslennikov, S.Y.; Kolobkova, E.V.; Bagrov, I.V. Intensification of photodecomposition of organics contaminations by nanostructured ZnO-SnO$_2$ coatings prepared by polymer-salt method. *Chem. Eng. Process-Process Intens.* **2019**, *142*, 107587. [CrossRef]
5. Matos, R.S.; Attah-Baah, J.M.; Monteiro, M.D.S.; Costa, B.F.O.; Mâcedo, M.A.; Da Paz, S.P.A.; Angélica, R.S.; de Souza, T.M.; Ţălu, S.; Oliveira, R.M.P.B.; et al. Evaluation of the photocatalytic activity of distinctive-shaped ZnO nanocrystals synthesized using latex of different plants native to the Amazon rainforest. *Nanomaterials* **2022**, *12*, 2889. [CrossRef]
6. Zaman, F.; Xie, B.; Zhang, J.; Gong, T.; Cui, K.; Hou, L.; Xu, J.; Zhai, Z.; Yuan, C. MOFs derived hetero-ZnO/Fe$_2$O$_3$ nanoflowers with enhanced photocatalytic performance towards efficient degradation of organic dyes. *Nanomaterials* **2021**, *11*, 3239. [CrossRef]
7. Khomutinnikova, L.L.; Evstropiev, S.K.; Danilovich, D.P.; Meshkovskii, I.K.; Bulyga, D.V. Structural engineering of photocatalytic ZnO-SnO$_2$-Fe$_2$O$_3$ composites. *J. Comp. Sci.* **2022**, *6*, 331. [CrossRef]

8. Ramos, P.G.; Sánchez, L.A.; Rodriguez, J.M. A review on improving the efficiency of photocatalytic water decontamination using ZnO nanorods. *J. Sol-Gel Sci. Technol.* **2022**, *102*, 105–124. [CrossRef]

9. Istomina, O.V.; Evstropiev, S.K.; Kolobkova, E.V.; Trofimov, A.O. Photolysis of diazo dye in solutions and films containing zinc and silver oxides. *Opt. Spectr.* **2018**, *124*, 774–778. [CrossRef]

10. Lu, Y.H.; Xu, M.; Xu, L.; Zhang, C.L.; Zhang, Q.P.; Xu, X.V.; Xu, S.; Ostrikov, K. Enhanced ultraviolet photocatalytic activity of Ag/ZnO nanoparticles synthesized by modified polymer-network gel method. *J. Nanopart. Res.* **2015**, *17*, 350. [CrossRef]

11. Dousthah, E.; Esmat, M.; Fukata, N.; Ide, Y.; Hanaor, D.A.H.; Assadi, M.H.N. MOF-derived nanocrystalline ZnO with controlled orientation and photocatalytic activity. *Chemosphere* **2022**, *303*, 134932. [CrossRef]

12. Ferreira, N.S.; Sasaki, J.M.; Silva JR, R.S.; Attah-Baah, J.M.; Macêdo, M.A. Visible light-responsive photocatalytic activity significantly enhanced by active (V_{Zn} + Vo^+) defects in self-assembled ZnO nanoparticles. *Inorg. Chem.* **2021**, *69*, 4475–4496. [CrossRef]

13. Gatou, M.-A.; Lagopati, N.; Vagena, I.-A.; Gazouli, M.; Pavlatou, E.A. ZnO Nanoparticles from Different Precursors and Their Photocatalytic Potential for Biomedical Use. *Nanomaterials* **2023**, *13*, 122. [CrossRef] [PubMed]

14. Gonullu, M.P.; Cergel, M.S.; Efkere, H.I.; Ates, H. Investigations of some physical properties of ALD growth ZnO films: Effect of crystal orientation on photocatalytic activity. *J. Mater. Sci. Mater. Electron.* **2021**, *32*, 12059–12074. [CrossRef]

15. Li, Y.; Zhang, W.; Niu, J.; Chen, Y. Mechanism of photogenerated reactive oxygen species and correlation with the antibacterial properties of engineered metal-oxide nanoparticles. *ACS Nano* **2012**, *6*, 5164–5173. [CrossRef] [PubMed]

16. Shelemanov, A.A.; Evstropiev, S.K.; Karavaeva, A.V.; Nikonorov, N.V.; Vasilyev, V.N.; Podruhin, Y.F.; Kiselev, V.M. Enhanced Singlet Oxygen Photogeneration by Bactericidal ZnO–MgO–Ag Nanocomposites. *Mater. Chem. Phys.* **2022**, *276*, 125204. [CrossRef]

17. Jiang, Y.; Li, S.; Wang, S.; Zhang, Y.; Long, C.; Xie, J.; Fan, X.; Zhao, W.; Xu, P.; Fan, Y.; et al. Enabling specific photocatalytic methane oxidation by controlling free radical type. *J. Am. Chem. Soc.* **2023**, *145*, 2698–2707. [CrossRef]

18. Turchi, C.S.; Ollis, D.F. Photocatalytic degradation of organic water contaminants: Mechanisms involving hydroxyl radical attack. *J. Catal.* **1990**, *122*, 178–192. [CrossRef]

19. Deng, Y. Developing a Langmuir-type excitation equilibrium equation to describe the effect of light intensity on the kinetics of the photocatalytic oxidation. *Chem. Eng. J.* **2018**, *337*, 220–237. [CrossRef]

20. Puma, G.L.; Salvadó-Estivill, I.; Obee, T.N.; Hay, S.O. Kinetics rate model of the photocatalytic oxidation of trichloroethylene in air over TiO_2 thin films. *Sep. Purif. Technol.* **2009**, *67*, 226–232. [CrossRef]

21. Belovolova, L.V. Reactive oxygen species in aqueous media (a review). *Opt. Spectr.* **2020**, *128*, 932–951. [CrossRef]

22. Hayyan, M.; Hashim, M.A.; AlNashef, I.M. Superoxide ion: Generation and chemical implications. *Chem. Rev.* **2016**, *116*, 3029–3085. [CrossRef]

23. Abebe, B.; Ananda Murthy, H.C.; Amare, E. Summary on adsorption and photocatalysis for pollutant remediation: Mini review. *J. Encapsulation Adsorpt. Sci.* **2018**, *8*, 225–255. [CrossRef]

24. Sun, X.; Xu, K.; Chatzitakis, A.; Norby, T. Photocatalytic generation of gas phase reactive oxygen species from adsorbed water: Remote action and electrochemical detection. *J. Environ. Chem. Eng.* **2021**, *9*, 104809. [CrossRef]

25. Saratovskii, A.S.; Bulyga, D.V.; Evstrop'ev, S.K.; Antropova, T.V. Adsorption and photocatalytic activity of the porous glass-ZnO-Ag composite and ZnO-Ag nanopowder. *Glass Phys. Chem.* **2022**, *48*, 10–17. [CrossRef]

26. Evstropiev, S.K.; Soshnikov, I.P.; Kolobkova, E.V.; Evstropyev, K.S.; Nikonorov, N.V.; Khrebtov, A.I.; Dukelskii, K.V.; Kotlyar, K.P.; Oreshkina, K.V.; Nashekin, A.V. Polymer-salt synthesis and characterization of MgO-ZnO ceramic coatings with the high transparency in UV spectral range. *Opt. Mater.* **2018**, *82*, 81–87. [CrossRef]

27. Sokolov, I.S.; Maslennikov, S.Y.; Evstropiev, S.K.; Mironov, L.Y.; Nikonorov, N.V.; Oreshkina, K.V. YAG:Ce^{3+} phosphor nanopowders and thin textured coatings prepared by polymer-salt method. *Opt. Eng.* **2019**, *58*, 027103. [CrossRef]

28. Evstropiev, S.K.; Karavaeva, A.V.; Petrova, M.A.; Nikonorov, N.V.; Vasilyev, V.N.; Lesnykh, L.L.; Dukelskii, K.V. Antibacterial effect of nanostructured ZnO-SnO_2 coatings: The role of microstructure. *Mater. Today Commun.* **2019**, *21*, 100628. [CrossRef]

29. Poongodi, G.; Ananan, P.; Mohan Kumar, R.; Jayavel, R. Studies on visible light photocatalytic and antibacterial activities of nanostructured cobalt doped ZnO thin films prepared by sol-gel coating method. *Spectrochim. Acta A Mol. Biomol. Spectr.* **2015**, *148*, 237–243. [CrossRef]

30. Boltenkov, I.S.; Kolobkova, E.V.; Evstropiev, S.K. Synthesis and characterization of transparent photocatalytic ZnO-Sm_2O_3 and ZnO-Er_2O_3 coatings. *J. Photochem. Photobiol. A Chem.* **2018**, *367*, 458–464. [CrossRef]

31. Talinungsang; Upadhaya, D.; Kumar, P.; Purkayastha, D.D. Superhydrophilicity of photocatalytic ZnO/SnO_2 heterostructure for self-cleaning applications. *J. Sol-Gel Sci. Technol.* **2019**, *92*, 575–584. [CrossRef]

32. Gayle, A.J.; Lenef, J.D.; Huff, P.A.; Wang, J.; Fu, F.; Dadheech, G.; Dasgupta, N.P. Visible-light-driven photocatalysts for self-cleaning transparent surfaces. *Langmuir* **2022**, *38*, 11641–11649. [CrossRef]

33. Hamrouni, A.; Moussa, N.; Parrino, F.; Di Paola, A.; Houas, A.; Palmisano, L. Sol-gel synthesis and photocatalytic activity of ZnO-SnO_2 nanocomposites. *J. Molec. Catal. A Chem.* **2014**, *390*, 133–141. [CrossRef]

34. Sabry, R.S.; Rahmah, M.I.; Aziz, W.J. A systematic study to evaluate effects of stearic acid on superhydrophobicity and photocatalytic properties of Ag –doped ZnO nanostructures. *J. Mat. Sci. Mater. Electron.* **2020**, *31*, 13382–13391. [CrossRef]

35. Zarei, S.; Hasheminiasari, M.; Masoudpanah, S.M.; Javadpour, J. Photocatalytic properties of ZnO/SnO_2 nanocomposite films: Role of morphology. *J. Mater. Res. Technol.* **2022**, *17*, 2305–2312. [CrossRef]

36. Xu, L.; Xian, F.; Zhang, Y.; Wang, W.; Qiu, K.; Xu, J. Synthesis of ZnO-decorated SnO_2 nanopowder with enhanced photocatalytic performance. *Optik* **2019**, *194*, 162965. [CrossRef]

37. Manoharan, C.; Pavithra, G.; Dhanapandian, S.; Dhamodaran, P.; Shanthi, B. Properties of spray pyrolised ZnO:Sn thin films and their antibacterial activity. *Spectrochim. Acta A Mol. Biomol. Spectrosc.* **2015**, *141*, 292–299. [CrossRef] [PubMed]

38. Tahir, D.; Ilyas, S.; Rahmat, R.; Heryanto, H.; Fahri, A.N.; Rahmi, M.H.; Abdullah, B.; Hong, C.C.; Kang, H.J. Enhanced visible-light absorption of Fe_2O_3 covered by activated carbon for multifunctional purposes: Tuning the structural, electronic, optical, and magnetic properties. *ACS Omega* **2021**, *6*, 28334–28346. [CrossRef] [PubMed]

39. Abbott, L.C.; Batchelor, S.N.; Oakes, J.; Lindsay Smith, J.R.; Moore, J.N. Spectroscopic studies of the intermolecular interactions of a Bis-Azo Dye, Direct Blue 1, on Di and trimerization in aqueous solution and in cellulose. *J. Phys. Chem. B* **2004**, *108*, 13726–13735. [CrossRef]

40. El-Bahy, Z.M.; Ismail, A.A.; Mohamed, R.M. Enhancement of titania by doping rare earth for photodegradation of organic dye (Direct Blue). *J. Hazard. Mater.* **2009**, *165*, 138–143. [CrossRef] [PubMed]

41. Volkova, N.A.; Evstropiev, S.K.; Istomina, O.V.; Kolobkova, E.V. Photolysis of diazo dye in aqueous solutions of metal nitrates. *Opt. Spectr.* **2018**, *124*, 489–493. [CrossRef]

42. Mohamed, G.R.M.; Mkhalid, I.A.; Al-Thabaiti, S.A.; Mohamed, M. Nano Cu metal doped on TiO_2-SiO_2 nanoparticle catalysts in photocatalytic degradation of direct blue dye. *J. Nanosci. Nanotechnol.* **2013**, *13*, 4975–4980. [CrossRef] [PubMed]

43. Ravichandran, K.; Vasanthi, M.; Thirumurugan, K.; Sakthivel, B.; Karthika, K. Annealing induced reorientation of crystallites in Sn doped ZnO films. *Opt. Mater.* **2014**, *37*, 59–64. [CrossRef]

44. Guo, L.; Yang, S.; Yang, C.; Yu, P.; Wang, J.; Ge, W.; Wong, G.K.L. Highly monodisperse polymer-capped ZnO nanoparticles: Preparation and optical properties. *Appl. Phys. Lett.* **2000**, *76*, 2901–2903. [CrossRef]

45. Tauc, J. Optical properties and electronic structure of amorphous Ge and Si. *Mater. Res. Bull.* **1968**, *3*, 37–46. [CrossRef]

46. Mang, A.; Reimann, K.; Rübenacke, S. Band gap, crystal field splitting, spin-orbit coupling and exciton binding energies in ZnO under hydrostatic pressure. *Solid State Commun.* **1995**, *94*, 251–254. [CrossRef]

47. Koike, K.; Hama, K.; Nakashima, I.; Takada, G.; Ogata, K.; Sasa, S.; Inoue, M.; Yano, M. Molecular beam epitaxial growth of wide bandgap ZnMgO alloy films on (111)-oriented Si substrate toward UV-detector applications. *J. Cryst. Growth* **2005**, *278*, 288–292. [CrossRef]

48. Ohtomo, A.; Kawasaki, M.; Koida, T.; Masubuchi, K.; Koinuma, H.; Sakurai, Y.; Yoshida, Y.; Yasuda, T.; Segawa, Y. $Mg_xZn_{1-x}O$ as a II-VI wide gap semiconductor alloy. *Appl. Phys. Lett.* **1998**, *72*, 2466. [CrossRef]

49. Toshihiro, D.; Yoshio, N. Formation and behavior of singlet molecular oxygen in TiO_2 photocatalysis studied by detection of near-infrared phosphorescence. *J. Phys. Chem. C* **2007**, *111*, 4420–4424.

50. Bell, S.; Will, G.; Bell, J. Light intensity effects on photocatalytic water splitting with a titania catalyst. *Int. J. Hydrogen Energy* **2013**, *38*, 6938–6947. [CrossRef]